Predicting phenotype using morphological cell responses to nanotopography

Marie F.A. Cutiongco[1], Bjørn S. Jensen[2], Paul M. Reynolds[1], Nikolaj Gadegaard[1,*]

[1]Divison of Biomedical Engineering, School of Engineering, University of Glasgow, Glasgow, United Kingdom
[2]School of Computing Science, University of Glasgow, Glasgow, United Kingdom
* corresponding author

Corresponding author:
Nikolaj Gadegaard, PhD
Division of Biomedical Engineering
Oakfield Avenue, Rankine Building
Glasgow, United Kingdom G12 8LT
Email: Nikolaj.Gadegaard@glasgow.ac.uk
Tel no: 01413305243

Keywords: machine learning, high content imaging, tissue engineering, quantitative structure and function, rational design

Abstract

Cells respond in complex ways to topographies, making it challenging to identify a direct relationship between surface topography and cell response. A key problem is the lack of informative representations of topographical parameters that translate directly into biological properties. Here, we present a platform to relate the effects of nanotopography on morphology to function. This platform utilizes the 'morphome', a multivariate dataset containing single cell measures of focal adhesions, the cytoskeleton, and chromatin. We demonstrate that nanotopography-induced changes in cell phenotype are uniquely encoded by the morphome. The morphome was used to create a Bayesian linear regression model that robustly predicted changes in bone, cartilage, muscle and fibrous tissue gene expression induced by nanotopography. Furthermore, the morphome effectively predicted nanotopography-induced phenotype within a complex co-culture microenvironment. Thus, the morphome enables the cell function-oriented exploration of new topographies, with potential applications in the development of novel surface-patterned biomaterials for tissue implants.

Introduction

Biomedical implants continue to be developed to improve patient outcomes. One way to enhance implant efficacy and tissue regeneration is to vary substrate texture with nanotopographies. Topographies at the cell-material interface are widely shown to direct cell behaviour: nanopillars change cell morphology[1]; nanogratings drastically alter lipid metabolism[2], and pluripotent[3-5] and multipotent cell differentiation[6]; nanogradients improve stem cell cardiomyogenic differentiation; and subtle changes to nanopit geometric arrangement switches human mesenchymal stem cells from multipotent to osteogenic fate[7-10]. Morphological responses to nanotopography are manifested through varying focal adhesion size[17-19], orientation[19-21], and composition[22,23] and changes in actin contractility and nuclear deformation[24].

A quantitative relationship exists between a material's physicochemical structure and its biological activity. Rational drug design has long relied on molecule solubility, ionisation and lipophilicity to predict activity[11]. Protein engineering has similarly modelled protein-peptide interactions from protein structure[12]. Cell metabolic activity correlates with synthetic polymer composition, glass transition temperature, and water contact angle[13]. Meanwhile, bacterial attachment can be predicted from descriptors of secondary ionic hydrocarbon chains[14]. In contrast to active biomolecules, the mechanotransductive effects of topography on cell response do not intuitively relate to topography length scale, isotropy, geometry, and polarity. This limits the discovery of functional topography to the screening of libraries for hits using a single, representative cell type[15-18]. Among its limitations (which include cost, inefficiency and the sampling of a small topography space), this screening approach disregards the cell specificity of response to nanotopogrpahy. Thus, it is vitally important to develop a systematic method to capture cell phenotypes induced by topography.

Here, we demonstrate a platform that encompasses cell phenotype and morphological response induced by nanotopography using image-based cellular features. We obtained measurements of focal adhesions, actin cytoskeleton and

chromatin, referred to here as the 'morphome', from single cells on nanotopographies. We observed a unique morphological signature based on cell identity and nanotopography in the morphome. We also identified changes in the transcription of myogenic, osteogenic, chondrogenic and fibroblastic genes across all combinations of cells and nanotopographies. We used a Bayesian linear regression model to directly relate the morphological and phenotypic changes induced by nanotopography. Using the morphome as predictors and without prior knowledge about the nanotopography, the model robustly predicted gene expression induced by nanotopography. A new morphome dataset from a co-culture of osteoblastic and fibroblastic cells verified that the model positively predicts bone tissue formation induced by nanotopography, even within a complex microenvironment. The lack of topography-specific parameters in the model and the presence of the mechanosensing machinery in all cell types highlights the broad applicability of this platform to many biomaterial and cell systems, thereby supporting the function-oriented exploration and rational design of new topographies.

Results

Measuring morphological cell responses to topography: the morphome

We used nanopit topographies consisting of 120 nm diameter, 100 nm depth and with a 300 nm centre-to-centre distance in a square array (SQ)[7], hexagonal array (HEX)[25-27], and arranged with centre-to-centre distance offset from 300 nm by 50 nm in both x and y directions (NSQ array)[7,8]. An unpatterned ('FLAT') surface was used as a control (Figure 1A).

We employed cells of the musculoskeletal system due to the diverse responses of muscle, bone, cartilage and fibrous cell types to nanotopographies[27-29]. Mouse myoblasts, osteoblasts, chondrocytes, fibroblasts, and pre-osteoblast[30] and pre-myoblast[31] progenitors, were grown on nanotopographies. Responses from combinations of each cell type on all nanotopographies were measured, providing 24 unique combinations of cell type and nanotopography (Figure S1). Effects of nanotopography on morphological characteristics such as cell and nuclear area, and

in pFAK activation levels, actin intensity and focal adhesion area were evident (Figure S2-S4).

Morphology (shape and geometry of different compartments), texture (spatial patterns of fluorescence), intensity (total fluorescence value), and radial distribution of intensity (measuring radial arrangement of fluorescence), were analysed for chromatin, actin, focal adhesion kinase (FAK) and phosphorylated FAK (pFAK) signals at day 2 of culture (Supplementary data). The morphome consisted of 624 single cell measurements ("features"), with 75 chromatin and nuclear features, 211 actin and whole-cell features, 168 FAK features, and 170 pFAK features (Figure 1B). Quantitative polymerase chain reaction (qPCR) was then used to assess changes in lineage marker expression induced by nanotopography by day 7. Machine learning was then applied on the morphome: (i) hierarchical clustering was used to uncover unique patterns of morphological features that distinguish cell type-specific responses on nanotopographies, and nanotopography-specific morphological changes induced within the cell; (ii) Bayesian linear regression was used to predict myogenic, osteogenic, chondrogenic and fibrogenic gene expression induced by nanotopography using the morphome as predictors (Figure 1D).

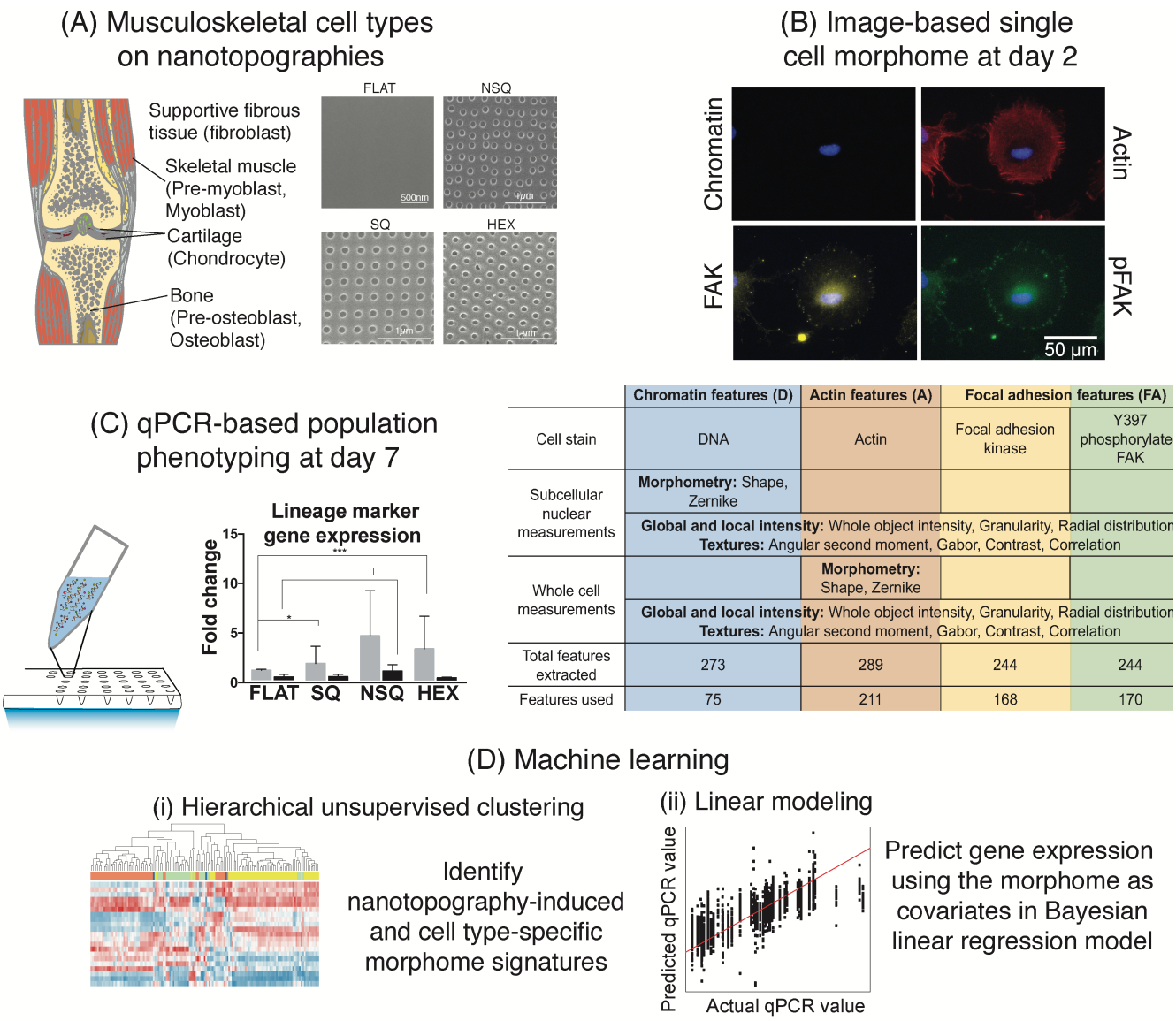

	Chromatin features (D)	Actin features (A)	Focal adhesion features (FA)	
Cell stain	DNA	Actin	Focal adhesion kinase	Y397 phosphorylate FAK
Subcellular nuclear measurements	**Morphometry:** Shape, Zernike			
	Global and local intensity: Whole object intensity, Granularity, Radial distribution **Textures:** Angular second moment, Gabor, Contrast, Correlation			
Whole cell measurements		**Morphometry:** Shape, Zernike		
	Global and local intensity: Whole object intensity, Granularity, Radial distribution **Textures:** Angular second moment, Gabor, Contrast, Correlation			
Total features extracted	273	289	244	244
Features used	75	211	168	170

Figure 1. An overview of the morphome platform for relating cell phenotype and morphological features changed by nanotopography. (A) Osteoblastic, myoblastic, chondroblastic and fibroblastic cells were cultured on nanotopographies to obtain 24 combinations of cell type and topography.(B) At day 2, various measures of chromatin (blue), actin (red), focal adhesion kinase (FAK, yellow) and phosphorylated FAK (pFAK, green) were obtained from images of single cells to create the 'morphome'. (C) At day 7, lineage-specific gene expression induced by nanotopography was measured using population-based qPCR. (D) Machine learning for data-driven exploration and model building using the morphome. (i) Hierarchical clustering uncovered unique patterns that delineate cell type and nanotopography within the morphome. (ii) Bayesian linear regression created a predictive model that related the morphome to gene expression and phenotype.

The morphome depicts unique cell signatures induced by nanotopographies

Patterns of nanotopography-induced morphological changes were visible from the morphome (Figure 2A). Immediately apparent were large blocks of actin, FAK and pFAK measurements with similar values within a cell type on a specific nanotopography. These features correspond to increasingly complex measures of texture, granularity and radial intensity distribution for chromatin, actin, FAK and pFAK (Table S1). Frequency of pixel gray levels measures texture and thus of homogeneity, with high texture values indicating coarseness. Granularity measures an object's coarseness, with higher values indicating heterogeneity of pixel intensities and coarser texture. The Zernike coefficient measures the spatial arrangement of intensity as it resembles the increasingly complex Zernike polynomials (Figure 2A). Interestingly, higher Zernike polynomials resemble the punctate shape and spatial distribution of focal adhesions[32].

Nanotopography induces cell type-specific gene expression changes

Gene expression was used to determine the effect of nanotopographies on cell phenotype (Figure S5). We discuss here the changes induced by nanotopography on lineage-specific gene expression relevant to the cell type. Pre-myoblasts showed significantly higher expression of the early lineage marker *MYOD1*, and of the late markers *MYOG* and *MYH7* when cultured on SQ surfaces relative to FLAT surfaces (Figure 2B-2D). Both pre-osteoblasts and osteoblasts showed increased expression of early (*RUNX2*, *SP7*) and late (*BGLAP*, *SPP1*) osteogenic markers when cultured on NSQ relative to FLAT (Figure 2E-2H), in line with previous studies[7,8,10,33]. Chondrocytes cultured on HEX showed increased expression of *COL2A1* (early marker) and *ACAN* (late marker) compared to those cultured on FLAT (Figure 2I-2K). Meanwhile, fibroblasts showed increased expression of pathogenic fibrosis markers, *TGFB1I1*, *COL3A1* and *ELN*[34,] on all nanotopographies compared with FLAT (Figure 2M-2O). In general, a cell type-specific response to nanotopography was observed. Each lineage was notably enhanced in a specific cell type and nanotopography combination: SQ stimulated the myoblast phenotype, NSQ enhanced the osteoblast phenotype, HEX stimulated the chondrocyte phenotype, while all surfaces except FLAT stimulated the fibrotic phenotype.

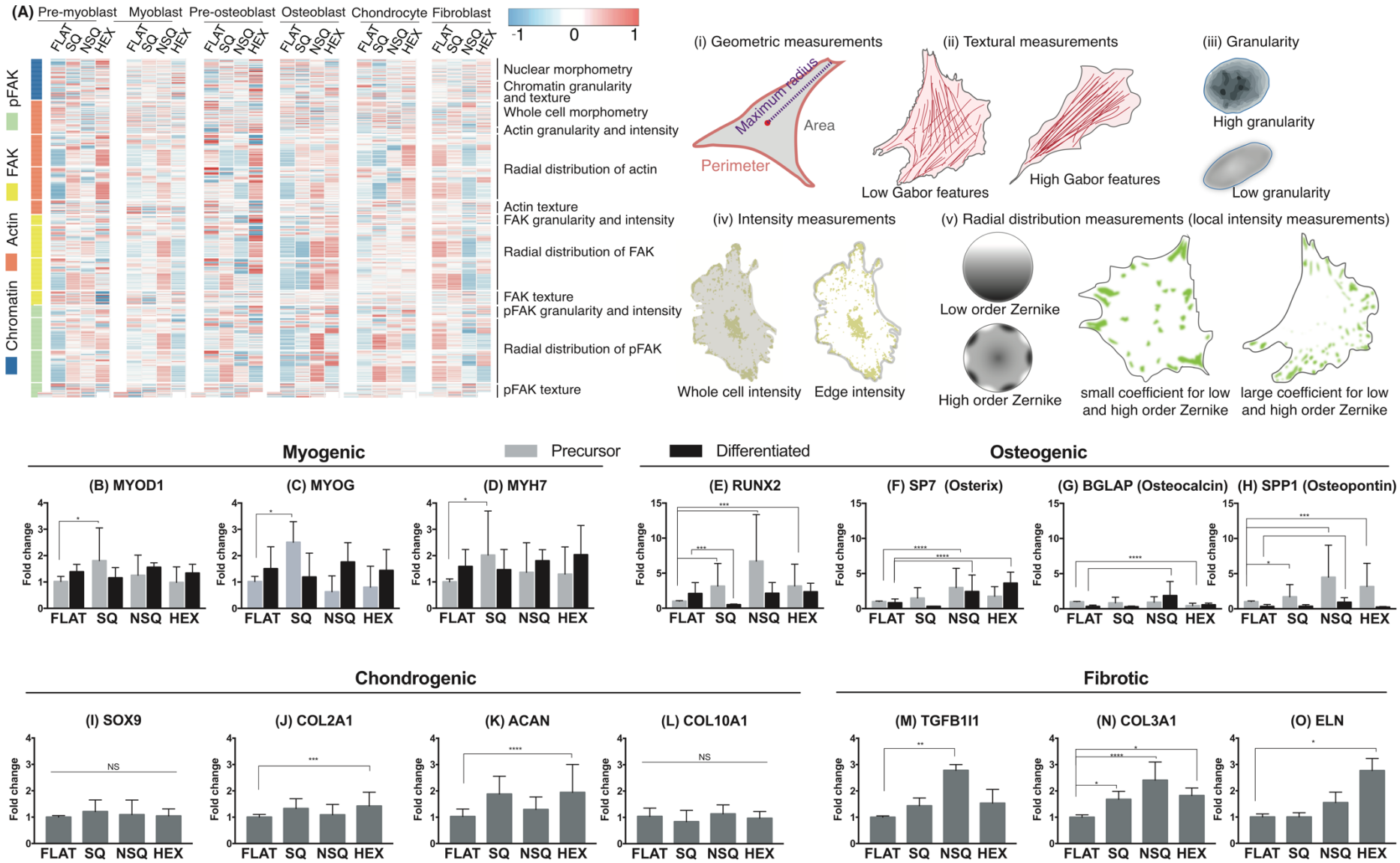
(A)
Pre-myoblast
Myoblast
Pre-osteoblast
Osteoblast
Chondrocyte
Fibroblast
FLAT SQ NSQ HEX
-1 0 1
pFAK
FAK
Actin
Chromatin
Nuclear morphometry
Chromatin granularity and texture
Whole cell morphometry
Actin granularity and intensity
Radial distribution of actin
Actin texture
FAK granularity and intensity
Radial distribution of FAK
FAK texture
pFAK granularity and intensity
Radial distribution of pFAK
pFAK texture
(i) Geometric measurements
Maximum radius
Area
Perimeter
(ii) Textural measurements
Low Gabor features
High Gabor features
(iii) Granularity
High granularity
Low granularity
(iv) Intensity measurements
Whole cell intensity
Edge intensity
(v) Radial distribution measurements (local intensity measurements)
Low order Zernike
High order Zernike
small coefficient for low and high order Zernike
large coefficient for low and high order Zernike
Myogenic
Precursor
Differentiated
Osteogenic
(B) MYOD1
(C) MYOG
(D) MYH7
(E) RUNX2
(F) SP7 (Osterix)
(G) BGLAP (Osteocalcin)
(H) SPP1 (Osteopontin)
Fold change
Chondrogenic
Fibrotic
(I) SOX9
(J) COL2A1
(K) ACAN
(L) COL10A1
(M) TGFB1I1
(N) COL3A1
(O) ELN
NS

Figure 2. Unique responses of cells to nanotopography at single-cell and population levels. (A) Heat map of the morphome across cell types and nanotopographies. The morphome consisted of 624 features that quantitatively measure the cell and nucleus geometries, as well as chromatin, actin, FAK, pFAK characteristics within single cells. The colour and intensity of each tile represents the average value of the feature for a particular cell type and nanotopography combination. Each feature has an average of 0 and a standard deviation of 1 after normalization across all cell types. Schematic diagrams of representative morphome features are included in (i) to (v). (B-O) QPCR of musculoskeletal genes in response to nanotopographies. Measurement of (B-D) myogenic markers from pre-myoblasts and myoblasts, (E-H) osteogenic markers from pre-osteoblasts and osteoblasts, (I-L) chondrogenic markers from chondrocytes, (M-O) fibrotic markers from fibroblasts on nanotopographies. Gene expression is listed left to right in order of increasing maturity for the given cell lineage. QPCR measurements shown here were normalized to the reference gene and cell type on FLAT. QPCR measurements across all 24 combinations of cell type and topography are shown in Figure S3. All qPCR measurements are given as mean ± standard deviation from 2 independent experiments (n=6). Significance levels obtained from one-way ANOVA with Tukey's post-hoc test, denoted by * ($p<0.05$), ** ($p<0.01$), *** ($p<0.001$), and **** ($p<0.0001$).

Distinct nanotopographical responses of single cells are reflected in the morphome

A subset of the morphome, consisting of 185 features, varied significantly across nanotopographies (Figure 3, Supplementary Data). Hierarchical clustering revealed that measurements of actin and pFAK radial distribution were most dissimilar to each other (Figure S6). Notably, the morphome of cells on FLAT already show that unique cell type signatures are manifested in the morphome.

Hierarchical clustering within each cell type reflected the cell type specificity of nanotopography response. Here, we highlight morphome for cell type and nanotopography combinations that induced highest lineage-specific gene expression. When compared to FLAT, pre-myoblasts on SQ showed high average values of: focal adhesion textures (Figure 3A, cluster 2); pFAK radial distribution (cluster 4); nuclear morphometry; and chromatin textures (cluster 4). The morphome of pre-myoblasts cultured on SQ reflects the need for FAK phosphorylation and for its preferential localization at stress fiber edges, which is necessary for myotube differentiation[36,37]. In contrast, myoblasts on SQ showed a particularly high average value for chromatin granularity and nuclear morphometry (cluster 4), and near-zero values for radial distribution of actin and of focal adhesions (cluster 1). High chromatin granularity observed for both pre-myoblasts and myoblasts on SQ denotes chromatin heterogeneity and condensation and transcriptional activity, which is reportedly higher prior to myotube formation[38,39].

Pre-osteoblasts on SQ and NSQ had high average values for pFAK radial distribution, intensity, granularity and texture, and high average values for granularity of chromatin and actin (clusters 1-5). However, pre-osteoblasts on SQ had higher order pFAK and FAK radial distribution than on NSQ, which induced the highest expression of osteogenic markers. The morphome of pre-osteoblasts grown on NSQ featured radially variable actin that resemble bone cells, which have high contractility and actin stress fibers[40].

For osteoblasts, the differences between the SQ and NSQ morphome were more prominent: NSQ induced lower average values of focal adhesion granularity, chromatin texture and nuclear morphometry (cluster 1), and higher average values for focal adhesion radial distribution (clusters 4-7) compared to SQ (Figure 3D). The osteoblast morphome on NSQ indicates that focal adhesions localize at regular intervals along the periphery, which is associated with osteogenesis[41]. Furthermore, changes in nuclear morphometry attributed to spreading after growth on stiff surfaces is also associated with osteogenic differentiation[42].

Chondrocytes on HEX, which significantly increased chondrogenic marker gene expression relative to FLAT, showed high average values of radial distribution, texture and granularity of actin and FAK, high average nuclear morphometry, and low average values of pFAK and chromatin measurements (Figure 3E, clusters 1-3). These characteristics reflect the morphological changes (including reduced contractility and stress fiber formation, increased cell circularity, and decreased cell spreading[40], low FAK phosphorylation[43] and poor focal adhesion formation[44]) of stem cells undergoing chondrogenesis.

The morphome of fibroblasts cultured on FLAT had high average values of both actin and focal adhesion measurements (Figure 3F, clusters 3 and 5). The highly uniform radial arrangement of focal adhesions and actin of cells on FLAT indicate reduced polarization and contractile morphology of fibroblasts activated to a fibrotic state[45]. Inflammation pathways are reportedly increased in fibroblasts on HEX[46], inducing low adhesion that is reflected in low actin and focal adhesion radial distribution (clusters 3-9). Fibroblasts grown on NSQ and HEX showed low average values of focal adhesion and actin radial distribution but high values when grown on SQ (cluster 2-5).

Overall, the morphome reflected cell-type specific responses to nanotopography. The morphome also exhibited patterns from different cell types (e.g. pre-osteoblasts vs osteoblasts) despite similarity in origin (Table S2). A multi-class logistic regression classifier was able to accurately distinguish 6 different cell types using the morphome (Figure S7). The radial arrangement of actin and focal adhesions were a

critical distinction of the musculoskeletal cell types induced by nanotopography, while the arrangement of actin fibers into stress fibers or into cortical, circular bundles provided information on various cell states.

We also clustered the morphome based on cell type (Figure S8-S9, Supplementary data). Patterns emerge in the morphome in direct response to nanotopography: NSQ induced high average values of pFAK radial distribution, texture and granularity; and HEX induced high average values of actin radial distribution. Correlation between the dendrograms confirm that the morphome clusters of different nanotopographies were dissimilar to each other (Table S3). The morphome enabled discrimination between 4 nanotopographies with 68% overall accuracy (87% classification rate for HEX) using multi-class logistic regression (Figure S10).

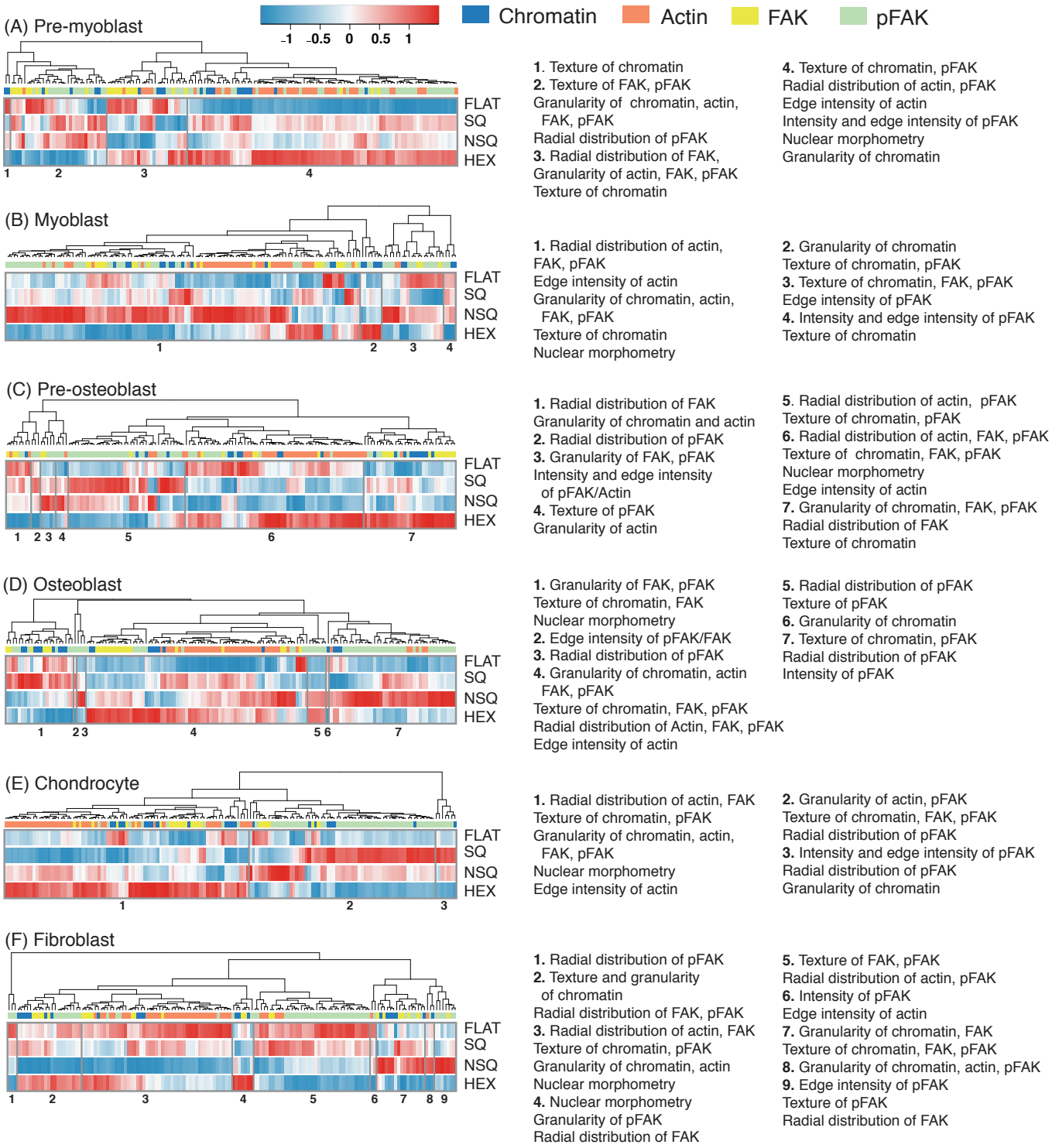

Figure 3. Nanotopography induced changes in single cells are evident in their morphomes. (A-F) Cell type-specific hierarchical clustering of the morphome averaged for each cell type. The total number of cells analyzed from two independent experiments are: (A) n=877 pre-myoblasts; (B) n=931 myoblasts; (C) n=644 pre-osteoblasts; (D) n=728 osteoblasts; (E) n=619 chondrocytes; and (F) n=1140 fibroblasts. The colour and intensity of each tile represents the average value of the feature. Each feature has an average of 0 and a standard deviation of 1 by normalizing within each cell type. The nanotopography specific morphome is made up of 21 chromatin, 42 actin, 23 FAK and 60 pFAK features. Features included were changed significantly across topographies ($p < 0.05$ using one-way ANOVA).

The morphome predicts nanotopography induced gene expression changes

The Spearman rank correlation revealed that varying degrees of correlation exist between morphome features and gene expression (Figure S11). We hypothesized that the features of the morphomes would sufficiently encompass cell phenotypes induced by nanotopography thus allowing prediction. We utilized Bayesian linear regression to predict gene expression using the morphome features as predictors (for the explicit model definition, see Materials and Methods). A Bayesian linear regression model reflects uncertainty in the estimation of regression weights compared to point value estimates using maximum likelihood regression. Gene expression was modelled independently of each other, thereby creating 14 different equations with variable weighting of the morphome features. Importantly, the model was trained without any prior knowledge of topography type, instead relying on the morphome to encode for this information.

The morphome clearly captured gene expression changes induced by nanotopography (Figure 4A). The heterogeneity inherent in single cells, usually uncaptured by population measurements of gene expression, are apparent in the variance of the predictions using the morphome and the model. The mean absolute error (MAE) for prediction of all genes was between 10% (for prediction of *MYOD1*, *MYOG* and *MYH7*) and 21% (for prediction of *COL3A1*, Table S4). Features with the highest contribution in predicting the 14 different genes were predominantly measurements of FAK texture and radial distribution, actin texture, and chromatin granularity (Figure S12, Supplementary data). pFAK activation, as indicated by pFAK/FAK intensity ratio, consistently contributed to the prediction of all 14 genes. pFAK was particularly important to the model due to its relevance in contractility induced by nanotopography[19], fibrosis and scar tissue formation[48], *in vitro* osteogenesis[49,50], and chondrogenic maintenance[43]. Through the variability in the model, we obtain realistic expectations of single cell predictions from population level measurements

The sensitivity and predictive power of the morphome was verified by iteratively training a model without one combination of cell type and topography (Figure 4E). Drastic increases in MAE were observed when lineage-specific genes were

predicted from models that excluded the particular cell type lineage being tested, regardless of nanotopography.

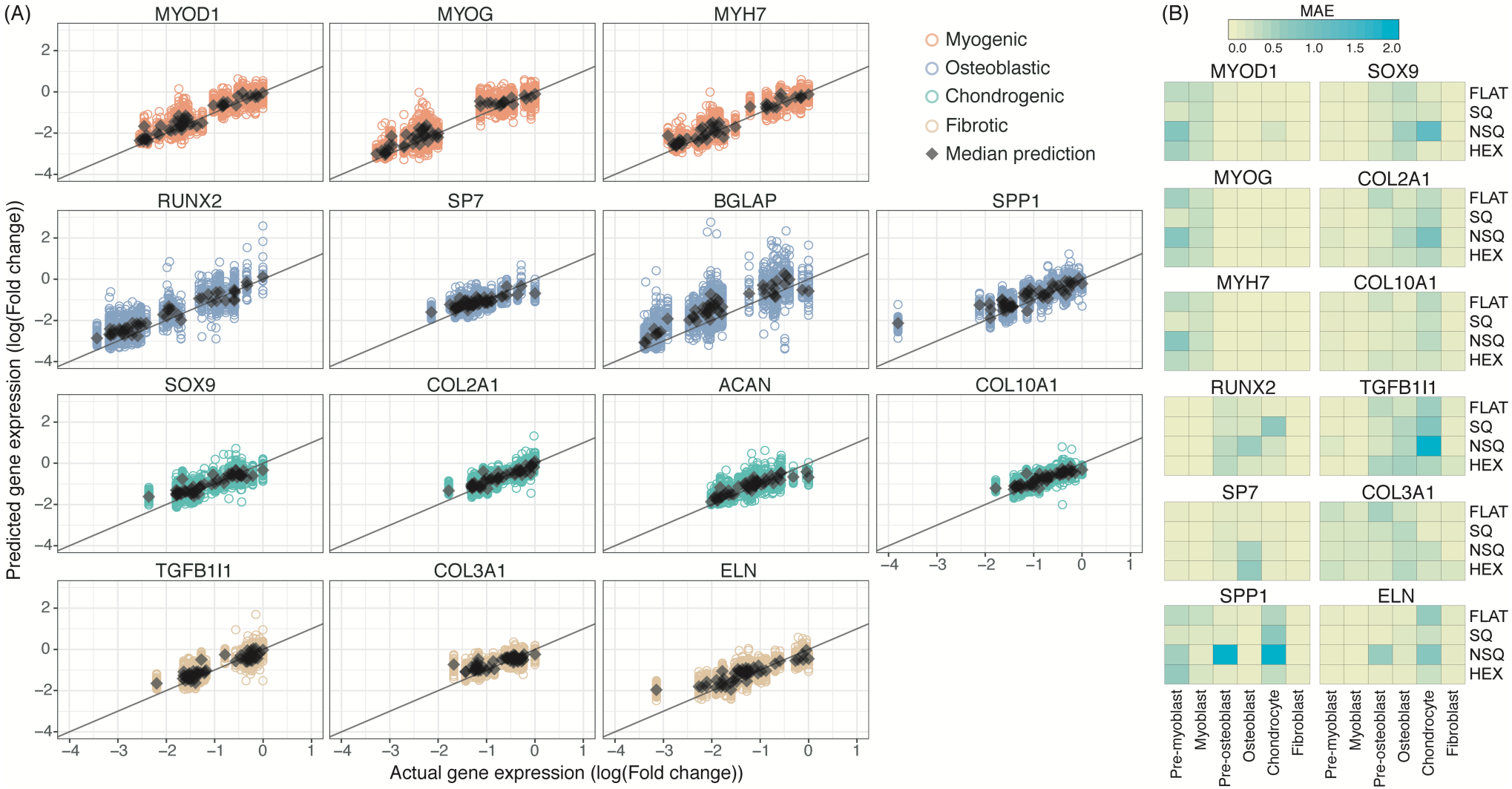
(A)
MYOD1
MYOG
MYH7
RUNX2
SP7
BGLAP
SPP1
SOX9
COL2A1
ACAN
COL10A1
TGFB1I1
COL3A1
ELN
Myogenic
Osteoblastic
Chondrogenic
Fibrotic
Median prediction
Predicted gene expression (log(Fold change))
Actual gene expression (log(Fold change))
(B)
MAE
0.0
0.5
1.0
1.5
2.0
FLAT
SQ
NSQ
HEX
Pre-myoblast
Myoblast
Pre-osteoblast
Osteoblast
Chondrocyte
Fibroblast

Figure 4. The morphome reliably predicts nanotopography-induced cell phenotype and gene expression from specific cell type and topography combinations. (A) The morphome was used to train a Bayesian linear regression model that predicted myogenic, osteogenic, chondrogenic, and fibrotic gene expression. The expression of each gene (response) was trained against linear combinations of morphome features (predictors) and without any prior knowledge on topography parameters. The linear regression model was trained using 60% of the dataset and tested using 40% of the data. Scatterplots show actual and predicted gene expression values by using the test set as input to the model. Mean absolute error (MAE) was obtained by averaging the differences between actual and predicted qPCR values. (B) Testing the predictive power of the morphome by leave-one-out validation. To test the predictive power and bias of the morphome, the linear regression model was retrained after exclusion of one combination of cell type and topography. The excluded cell type and topography dataset was used for prediction, from which MAE was calculated. The tile position denotes the cell type and nanotopography combination that was excluded in the model and used for testing, while the color of each tile denotes the MAE.

1

The morphome encompasses cell response to topography within a complex environment

We demonstrate the application of the linear regression model by predicting the outcome of pre-osteoblasts and fibroblasts co-cultured on nanotopographies. A new morphome were obtained from all cells on the entire nanotopography (Figure S13). This co-culture morphome was then used in the linear regression model to predict gene expression (Figure S14).

For visualization, the sum of predicted osteogenic (*RUNX2, SP7, BGLAP* and *SPP1*) and fibrotic (*TGFB1I1, COL3* and *ELN*) genes was plotted against the spatial coordinates of the pre-osteoblasts and fibroblasts. Osteogenic gene expression was highest on NSQ, which also induced concentrated areas of highly expressing cells (Figure 5A). These areas might represent hotspots of osteogenic paracrine signaling induced by the NSQ nanotopography[9]. In contrast, osteogenic gene expression was low and homogenous on the FLAT, SQ and HEX topographies.

Fibrotic gene expression showed more spatial variability across the nanotopographies but was also maximized on the NSQ nanotopography, and largely overlaps with the spatial pattern of osteogenic gene expression (Figure 5B). This is attributable to the synergistic interaction of osteoblasts and fibroblasts on osteogenic differentiation and mineralization[51]. The predicted effect of high osteogenic gene expression induced by NSQ was verified in the increased mineralization and bone tissue formation compared to FLAT at 28 days (Figure S15). Our results demonstrate the capability of the morphome-based platform to capture topography induced responses within complex microenvironments reminiscent of *in vivo* settings.

The morphome and its application in the linear regression model enables the simultaneous assessment of morphological and functional effects of nanotopography at the single cell level. For instance, nanotopographies show no discernible effects on nuclear perimeter or on the ratio of pFAK/FAK intensity (Figure 5C). Yet there was a clear gradient in predicted osteogenic gene expression: as the nucleus reduced in size and pFAK activation rises, osteogenic gene expression increased. This gradient was less clear with fibrotic gene expression. However, the

nanotopographies have discernably different effects on actin and pFAK radial distribution, with cells on SQ showing the lowest values (Figure 5D). These nanotopography-specific cell clusters also revealed low osteogenic gene expression yet high fibrotic gene expression. The morphome clearly enables new insight into single cell responses induced by nanotopography.

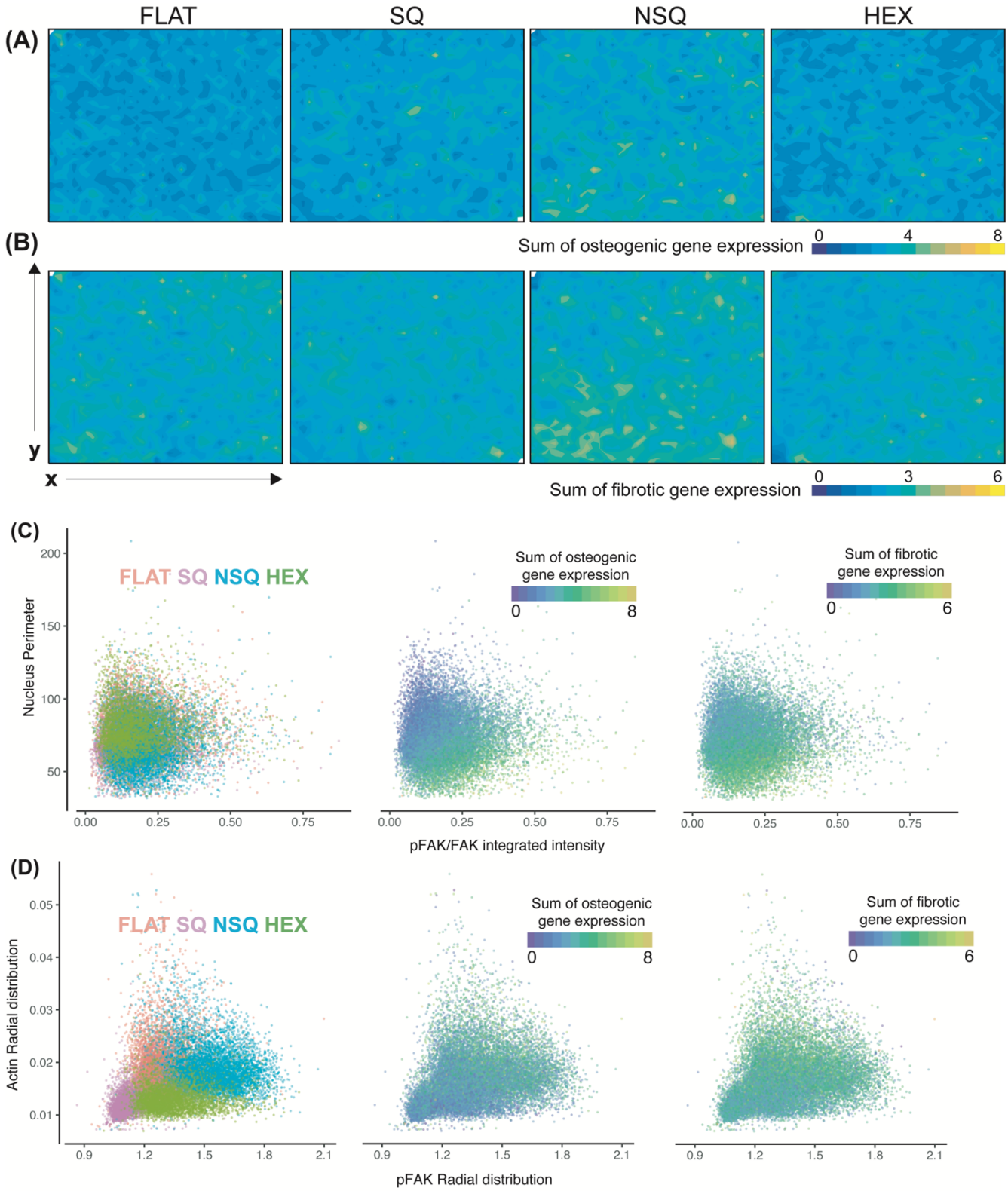

Figure 5. Morphological and functional response of single cells induced by nanotopography. (A-B) Predicted functional response of a pre-osteoblast and fibroblast co-culture to nanotopography. Contour plots show the sum of predicted (A) osteogenic (RUNX2, SP7, BGLAP, SPP1) and (B) fibrotic (TGFB1I1, COL3, ELN) gene expression for individual cells on

FLAT, SQ, NSQ and HEX topographies. Pre-osteoblast and fibroblast cells were co-cultured on FLAT, SQ, NSQ and HEX nanotopographies for 2 days, and their morphome obtained from the entire grid. This new morphome was then used as input in the linear regression model (shown in Figure 4) to predict gene expression. A 2.12 mm x 2.12 mm grid was imaged for each nanotopography. X and Y axes of each contour plot shows are spatial coordinates on the nanotopogrpahy substrate. (C-D) Morphological and functional information at the single-cell level is provided by the morphome. Each dot in the plot denotes a single cell. The morphome enables simulataneous analysis of morphological and functional changes induced by nanotopography at the single cell. N ≥ 5000 cells per topography.

Discussion

In this study, we present a system that robustly encodes nanotopography parameters into functional cell specific output. The morphome, which is the collective morphological measurements of chromatin, actin and focal adhesions within single cells, were found to manifest nanotopography-induced changes in cell morphology and cell function. The information encoded in the morphome underpinned the performance of a Bayesian linear regression model for predicting gene expression.

Focal adhesion complexes are the primary mechanosensing machinery of the cell that respond to the biophysical microenvironment. Focal adhesion assembly or confinement induced by nanotopography allows spontaneous actin cytoskeleton assembly, nucleus deformation, and cell fate determination[24,52,53]. Cells also change and control their microenvironment, thereby dictating focal adhesion and cellular characteristics to varying degrees[54,55]. Focal adhesion growth is particularly significant in sensing nanoscale changes in ligand arrangement, as this supports force redistribution throughout the cell [56]. This reciprocity between the nanotopographical microenvironment, focal adhesions, cytoskeleton and chromatin, and cell function underline the platform presented in this study.

Our results demonstrate that quantitative measures of high-level cell response to nanotopography emerge from the morphome. The morphome-based platform reported here offers two unique advantages. First, the design parameters of the nanotopographies were explicitly excluded in predicting cell function. To use structural information from topography (e.g. depth, diameter, pitch, geometry,

isotropy, roughness) considerably limits the dataset to only a handful of descriptors. As opposed to polymer-based biomaterials that contain easily interpretable physicochemical properties derived from chemical structure, the effects of topography parameters on hydrophobicity, serum adsorption and cell attachment are less well understood and quantified. Instead, the information contained in the morphome encompass both topography and cell function. Furthermore, by creating a general model that is independent of topographical parameters, this approach can be easily applied to predict cell functions induced by new nanotopographies. Second, in this approach, gene expression-based measures of cell phenotype determined the specialized function of cells. In contrast to our system, many quantitative structure and function relationship studies of polymeric biomaterials have focused only on unspecialized cellular behaviours, such as adhesion and metabolic activity[13,14]. Since gene expression is highly scalable, the linear regression model can be adapted to predict other cell behaviours or phenotypes. This also ensures that the morphome supports a function-focused exploration of the topography space and the rational design of topographies, as opposed to the currently used trial-and-error screening approach.

Our data reveals that the morphome can also manifest information on the stage within the cellular lineage commitment timeline. The morphome easily captured the higher levels of mature gene expression in cells farther along lineage commitment compared to precursor cells. Additionally, our co-culture experiments robustly predicted the osteogenic properties induced by NSQ. The elevated level of predicted osteogenic gene expression was supported by high mineralization on NSQ after 28 days of culture. Our results suggest that the morphome can manifest cellular changes induced by nanotopography, as well as changes driven by chemical or paracrine cues. This property of the morphome can be exploited to predict cell behavior in settings that recapitulate in vivo-like environments with numerous microenvironmental signals.

The co-culture experiment also demonstrated that the morphome dataset encompasses, at high resolution, structural, functional and spatial information. Structural information is crucial for determining how cells look, a highly valuable

feature that can also be used to study drug- and disease-induced cell perturbation. The functional information – represented by changes in the expression of 14 different genes – can be observed at single-cell level, reflecting spatial resolution that is invaluable in high-throughput formats. When developed as an automated platform that executes topography production, cell seeding and staining, image acquisition, morphome extraction and gene expression prediction, this approach could increase screening efficiency and make it more cell function-oriented.

Clearly, morphome capture is crucial to the ability of the linear regression model to predict nanotopography induced cell function. While population-level measures of gene expression strongly indicate cell function, they introduce a measure of uncertainty and biological variability into the linear regression model. Thus, a one-to-one relationship between the morphome and cell function is essential to develop. Non-destructive microscopic and molecular tools[57] that combine spatial and structural information from the morphome with single-cell functional assays are vitally important for establishing quantitative topography structure- and cell-function relationships using the morphome. However, the use of routine methods, such as high-content imaging and qPCR, permits any lab to measure the morphome and to model it against the cell function in question.

By generating a multivariate morphome dataset and combining it with machine learning, we have created a powerful platform for relating topography structure to cell function. The predictive power of the Bayesian linear regression model we have developed easily lends to sequential experimental design by exploiting the uncertainty and variability within the model[1,2]. This platform can ultimately be used to guide the testing and exploration of new topographies.

Materials and methods

Polycarbonate surfaces with nanotopography

Surfaces patterned with 120 nm diameter and 100 nm depth nanopits were fabricated on polycarbonate using injection molding[60]. The following nanotopographies were used: surfaces without nanopits (FLAT); nanopits in a

square array with 300 nm center-to-center spacing (SQ); nanopits in a square array with approximately 300 nm center-to-center spacing distorted by 50 nm in both x and y directions (NSQ); nanopits in a hexagonal array with 300 nm center-to-center spacing (HEX). Samples were cleaned in 70% ethanol and dried before treating with O_2 plasma at 120 W for 1.5 mins. Samples were sterilized using UV light in biological safety cabinet for at least 20 mins before cell seeding.

Cell culture

Mouse fibroblast cell line NIH3T3 (ATCC) was cultured in reduced sodium bicarbonate content (1.5 g/L) Dulbecco's modified eagle's medium with (DMEM) supplemented with L-glutamate (2mM), 10% bovine calf serum, and 1% penicillin-streptomycin. Mouse C2C12 myoblasts (ATCC) were cultured in DMEM with 20% FBS and 1% penicillin-streptomycin, and differentiated into skeletal muscle using DMEM supplemented with 2% horse serum and 1% penicillin streptomycin. Mouse primary chondrocytes were cultured in minimum essential medium alpha (MEMα) with nucleosides, ascorbic acid, glutamate, sodium pyruvate supplemented with 10% FBS and 1% penicillin-streptomycin. Mouse MC3T3 cells (ATCC) were cultured in MEMα with nucleosides and L-glutamine without ascorbic acid and supplemented with 10% FBS and 1% penicillin-streptomycin. To differentiate MC3T3 into osteoblasts, MC3T3 media was supplemented with 10 nM dexamethasone, 50 µg/ml ascorbic acid and 10 mM beta-glycerophosphate[61]. Lineage committed progenitor cells, referred to here as pre-osteoblasts and pre-myoblasts, were also included in the study to mimic the osteogenic and myogenic regeneration in the adult tissue[30,31].

Cell seeding

Cells were harvested from flasks using trypsin in versene buffer and spun down at 400 x g for 5 minutes. NIH3T3 and MC3T3 cells were resuspended in complete media and seeded at 4000 cells/cm^2. Chondrocytes and C2C12 were seeded at 2500 cells/cm^2. Cells were seeded at different densities to ensure single cells at approximately 30% confluency on each surface after 2 days culture. To ensure homogeneity of seeding, cells were seeded using a cell seeder that controlled fluid flow. For co-culture studies, MC3T3 and NIH3T3 cells were simultaneously seeded

at 2000 cells/cm^2 per cell type in MC3T3 growth media. All cells were grown for 2 days on nanotopographies before fixation for immunofluorescence staining.

Quantitative polymerase chain reaction (qPCR)

After 6 days, total RNA was obtained from lysed cells according to manufacturer's instructions (Promega ReliaPrep Cell Miniprep kit). Gene expression was measured directly from 5 ng RNA using a one-step RT PCR kit with SYBR dye (PrimerDesign). qPCR was run on the BioRad CFX96 platform. Relative gene expression was normalized to the 18S ribosomal RNA reference gene. A list of the forward and reverse primers used to study different mouse genes is given in Table S5. Bar charts for qPCR data were obtained using GraphPad Prism (v7.0). One-way ANOVA with Tukey's post hoc test for multiple comparisons was performed to determine the effect of nanotopography on gene expression compared with FLAT. Statistical significance was considered at $p < 0.05$.

Immunofluorescence staining

After 2 days, cells on surfaces were fixed with 4% paraformaldehyde solution in phosphate buffered saline (PBS) at 4°C for 15 minutes. Fixed cells were then permeabilized and blocked with 10% goat serum and 2% bovine serum albumin in PBS for 1 hour at room temperature. Surfaces were stained with the following primary antibodies overnight at 4°C: pFAK Y397 (Abcam 39967, 1:400) and FAK (ThermoScientific 396500, 1:400). Afterwards, Alexa Fluor-conjugated secondary antibodies (ThermoScientific, 1:500) against the host species of the primary antibody were used. Alexa Fluor 549 conjugated phalloidin (ThermoScientific, 1:200) were used to structuralize the actin cytoskeleton. Cells were also stained with DAPI (ThermoScientific) to structuralize nuclei. All surfaces were mounted on 0.17 μm thick Glass coverslips with ProLong mounting medium (ThermoScientific) and dried overnight at 4°C before imaging.

Image acquisition and feature extraction

For single-cell population studies, monochrome images of each fluorophore were obtained at 40X magnification (numeric aperture 1.3) using the EVOS FL1 System (ThermoScientific). For co-culture studies, the entire field per nanotopography was

imaged and stitched through an automated microscope (EVOS FL2 Auto) with a 40X magnification. All images from one cell type were obtained using the same camera and light settings. Afterwards, images were analysed using CellProfiler (v2.4.0, The Broad Institute). Image processing, including illumination correction and channel alignment, was performed across each independent experiment and each cell type[62]. Nucleus and cell body were segmented from each cell in each image. Shape or morphometric measurements, total and local intensities and textures of chromatin, actin, pFAK and FAK were obtained using built-in object measurement modules in CellProfiler[63].

Machine learning and multivariate analysis

The morphome initially consisted of a total of 1050 measurements obtained from single cells. Morphome measurements from single-cell populations were combined and were scaled by subtracting the mean and normalizing by the standard deviation of the entire data set. Morphome data from co-culture studies were similarly scaled and normalized using the mean and standard deviation from the initial dataset consisting of homogeneous cell populations. Prior to machine learning, features with zero variance within each batch (e.g. Zernike Phase measurements) were removed from the data set. A Pearson correlation method at significance level 90% was used to remove features with correlation higher than 0.9 without significantly reducing total data variance (Figure S16) using the *KMDA* package[64]. After preprocessing, 624 morphome features were used further in the study. To determine the features that were significantly varied either across nanotopography or cell type, a one-way ANOVA was performed (KNIME v3.3.0). The intersection of nanotopography-specific and cell type-specific features were obtained. Hierarchical clustering was performed using Spearman correlation as a distance metric and an average linkage method for cluster linkage using *gplots* package[65]. Cluster membership and stability was obtained from silhouette analysis using the *cluster* package[66]. Dendrogram correlation was performed using *corrplot* package[67].

Bayesian linear log-Normal regression

Only morphome features with an absolute Spearman correlation coefficient ≥ 0.7 against all examined expression markers were used in the linear regression model

(Supplementary data). The linear regression model used 243 morphome features, containing 22 nuclear morphometry and chromatin, 71 actin, 75 FAK and 75 pFAK measurements, as predictors of the model. Each replicate of the qPCR data was propagated across each replicate of the single-cell morphome data. For each gene analysed, data were rescaled from 0 to 1 by normalizing to the maximum gene expression.

Linear regression was performed as a simple approximation of the relationship between the morphome and myogenic, osteogenic, chondrogenic and fibrotic gene expression. Established Bayesian inference methods were used to determine the probabilities of observing gene expression with a given morphome set. We consider a linear model where expression of one gene (response y) was predicted through a linear combination of the morphome features (predictors X) transformed by the inverse identity link function. We assume that y follows a log Normal distribution parametrized by the mean μ and variance σ_i^2:

$$y_i \sim Lognormal(\mu_i, \sigma_i^2)$$

And that μ is a linear function of X parametrized by β:

$$\mu_i = \alpha + \beta_0 + \beta_1 X_1 + \beta_2 X_2 + \cdots + \beta_n X_n$$

All model parameters β were assumed *a priori* to come from a normal distribution, parametrized by mean and standard deviation:

$$\beta \sim Normal(0, 2)$$

Each gene was trained independently resulting in 14 different linear regression equations. A 60%-40% training and test split for Bayesian linear regression was performed randomly and with stratification using the *caret* package for R[68]. The Bayesian linear model was created using the *brms* package for R[69], which utilizes the Hamiltonian Markov Chain Monte Carlo sampler for estimation of the posterior distribution of β. Bayesian linear modelling was carried out using with 1000 warm-up

iterations and 1000 sampling iterations within each chain for 3 independent chains. All models were confirmed to converge to the equilibrium distribution by confirming potential scale reduction statistic split-$\hat{R} \geq 1$, effective sample size was smaller than total sample size and low autocorrelation. Predicted gene expression was performed by using the test set or the morphome obtained from the co-culture study as input to the linear model. Predicted values were averaged across 50 draws from the posterior distribution.

To determine the predictive power of the morphome, a specific combination of cell type, topography and replicate were iteratively omitted and the remaining dataset was used to refit new models. Thus, 576 additional models were created to test 24 different cell type combinations across 12 genes and 2 replicates. The predictive quality of the models was assessed by predicting the expression of all 14 genes from the omitted cell type, topography and replicate dataset. We report the mean absolute error (MAE) of qPCR prediction for each cell type and topography combination averaged across 2 replicates. MAE was calculated as the average across all absolute differences between predicted and actual gene expression.

Statistics, visualization and software

Statistical analysis and machine learning were performed using statistical software R (v3.4.3) and its graphical interface RStudio (v1.0)[70]. Scatterplots, boxplots and histograms were generated using *ggplot2* in R[71]. Pearson correlation, Spearman rank correlation and Bayesian linear regression were performed in R (v3.4). Interpolation of x and y coordinates and sum of predicted osteogenic or fibrotic gene expression was performed using bivariate interpolation of a regularly gridded dataset using *akima* package[72]. Afterwards, the contour plots were created using the *fitted.contour* function in the base package of R, with the nuclear centroid position used as spatial coordinates of the cell. Barcharts and one-way ANOVA analysis of qPCR values were obtained using GraphPad Prism (v7.0a).

Acknowledgements

We acknowledge ERC funding through FAKIR 648892 Consolidator Award. MFAC is financially supported by the University of Glasgow MG Dunlop Bequest, College of Science and Engineering Scholarship, and FAKIR consolidator award. We acknowledge the James Watt Nanofabrication Centre for fabrication work, and Steen Lillelund for initiating the machine learning work. We thank Julie Russell for her contribution to the qPCR, Carmen Huesa for providing the primary cartilage cells and Rachel Love for the injection moulding of nanopatterned polycarbonate surfaces.

Author contributions

MFAC, PMR and NG designed the biological experiments. MFAC and BSJ designed the machine learning analysis. MFAC carried out imaging, image analysis, qPCR, machine learning. PMR fabricated and characterized the nanotopographical surfaces. MFAC, BSJ, PMR and NG wrote the manuscript. All authors have read and approved the manuscript before submission.

Disclosure of competing financial interests

The authors have no competing financial interests to disclose.

References

1. Reynolds, P. M., Pedersen, R. H., Riehle, M. O. & Gadegaard, N. A Dual Gradient Assay for the Parametric Analysis of Cell-Surface Interactions. *Small* **8,** 2541–2547 (2012).
2. Di Rienzo, C. *et al.* Unveiling LOX-1 receptor interplay with nanotopography: mechanotransduction and atherosclerosis onset. *Sci. Rep.* **3,** 1–8 (2013).
3. Chan, L. Y., Birch, W. R., Yim, E. K. F. & Choo, A. B. H. Temporal application of topography to increase the rate of neural differentiation from human pluripotent stem cells. *Biomaterials* **34,** 382–392 (2013).
4. Tan, K. K. B. *et al.* Enhanced differentiation of neural progenitor cells into neurons of the mesencephalic dopaminergic subtype on topographical patterns. *Biomaterials* **43,** 32–43 (2015).
5. Rasmussen, C. H. *et al.* Enhanced Differentiation of Human Embryonic Stem Cells Toward Definitive Endoderm on Ultrahigh Aspect Ratio Nanopillars. *Adv. Funct. Mater.* **26,** 815–823
6. Yim, E. K. F., Pang, S. W. & Leong, K. W. Synthetic nanostructures inducing differentiation of human mesenchymal stem cells into neuronal lineage. *Exp. Cell Res.* **313,** 1820–1829 (2007).

7. McMurray, R. J. *et al.* Nanoscale surfaces for the long-term maintenance of mesenchymal stem cell phenotype and multipotency. *Nature Materials* **10,** 637–644 (2011).
8. Dalby, M. J. *et al.* The control of human mesenchymal cell differentiation using nanoscale symmetry and disorder. *Nature Materials* **6,** 997–1003 (2007).
9. Tsimbouri, P. M. *et al.* Using Nanotopography and Metabolomics to Identify Biochemical Effectors of Multipotency. *ACS Nano* **6,** 10239–10249 (2012).
10. Yang, J. *et al.* Nanotopographical Induction of Osteogenesis through Adhesion, Bone Morphogenic Protein Cosignaling, and Regulation of MicroRNAs. *ACS Nano* **8,** 9941–9953 (2014).
11. Luan, F. & (null), M. C. in *Recent Trends on QSAR in the pharmaeutical perceptions* (ed. Khan, M.) 194–241 (books.google.com, 2012). doi:10.2174/9781608053797112010194
12. Jenson, J. M. *et al.* Peptide design by optimization on a data-parameterized protein interaction landscape. *Proc. Natl. Acad. Sci. U.S.A.* **592,** 201812939 (2018).
13. Kholodovych, V. *et al.* Accurate predictions of cellular response using QSPR: a feasibility test of rational design of polymeric biomaterials. *Polymer* **45,** 7367–7379 (2004).
14. Hook, A. L. *et al.* Combinatorial discovery of polymers resistant to bacterial attachment. *Nat Biotechnol* **30,** 868–875 (2012).
15. Moe, A. A. K. *et al.* Microarray with Micro- and Nano-topographies Enables Identification of the Optimal Topography for Directing the Differentiation of Primary Murine Neural Progenitor Cells. *Small* **8,** 3050–3061 (2012).
16. Kukumberg, M., Yao, J. Y., Neo, D. J. H. & Yim, E. K. F. Microlens topography combined with vascular endothelial growth factor induces endothelial differentiation of human mesenchymal stem cells into vasculogenic progenitors. *Biomaterials* **131,** 68–85 (2017).
17. Unadkat, H. V. *et al.* An algorithm-based topographical biomaterials library to instruct cell fate. *Proc. Natl. Acad. Sci. U.S.A.* **108,** 16565–16570 (2011).
18. Ankam, S. *et al.* Substrate topography and size determine the fate of human embryonic stem cells to neuronal or glial lineage. *Acta Biomaterialia* **9,** 4535–4545 (2013).
19. Teo, B. K. K. *et al.* Nanotopography Modulates Mechanotransduction of Stem Cells and Induces Differentiation through Focal Adhesion Kinase. *ACS Nano* **7,** 4785–4798 (2013).
20. Zhou, Q. *et al.* Directional nanotopographic gradients: a high-throughput screening platform for cell contact guidance. *Sci. Rep.* **5,** 16240 (2015).
21. Balaban, N. Q. *et al.* Force and focal adhesion assembly: a close relationship studied using elastic micropatterned substrates. *Nature Cell Biology* **3,** 466–472 (2001).
22. Kulangara, K., Yang, Y., Yang, J. & Leong, K. W. Nanotopography as modulator of human mesenchymal stem cell function. *Biomaterials* **33,** 4998–5003 (2012).

23. Cavalcanti-Adam, E. A. *et al.* Cell Spreading and Focal Adhesion Dynamics Are Regulated by Spacing of Integrin Ligands. *Biophysical Journal* **92,** 2964–2974 (2007).
24. Natale, C. F., Ventre, M. & Netti, P. A. Tuning the material-cytoskeleton crosstalk via nanoconfinement of focal adhesions. *Biomaterials* **35,** 2743–2751 (2014).
25. Dalby, M. J. *et al.* Nanomechanotransduction and interphase nuclear organization influence on genomic control. *J. Cell. Biochem.* **102,** 1234–1244 (2007).
26. Dalby, M. J., Gadegaard, N. & Wilkinson, C. D. W. The response of fibroblasts to hexagonal nanotopography fabricated by electron beam lithography. *J Biomed Mater Res A* **84,** 973–979 (2008).
27. Dalby, M. J. *et al.* Group analysis of regulation of fibroblast genome on low-adhesion nanostructures. *Biomaterials* **28,** 1761–1769 (2007).
28. Dalby, M. J., Riehle, M. O., Yarwood, S. J., Wilkinson, C. D. W. & Curtis, A. S. G. Nucleus alignment and cell signaling in fibroblasts: response to a micro-grooved topography. *Exp. Cell Res.* **284,** 272–280 (2003).
29. Allan, C. *et al.* Osteoblast response to disordered nanotopography. *J Tissue Eng* **9,** 204173141878409–7 (2018).
30. Quarles, L. D., Yohay, D. A., Lever, L. W., Caton, R. & Wenstrup, R. J. Distinct proliferative and differentiated stages of murine MC3T3-E1 cells in culture: an in vitro model of osteoblast development. *Journal of Bone and Mineral Research* **7,** 683–692 (1992).
31. Wagers, A. J. & Conboy, I. M. Cellular and molecular signatures of muscle regeneration: current concepts and controversies in adult myogenesis. *Cell* **122,** 659–667 (2005).
32. Kumar, R. M. & Sreekumar, K. A survey on image feature descriptors. *Int J Comput Sci Inf Technol* (2014).
33. Tsimbouri, P. *et al.* Nanotopographical effects on mesenchymal stem cell morphology and phenotype. *J. Cell. Biochem.* **115,** 380–390 (2014).
34. Van De Water, L., Varney, S. & Tomasek, J. J. Mechanoregulation of the Myofibroblast in Wound Contraction, Scarring, and Fibrosis: Opportunities for New Therapeutic Intervention. *Advances in Wound Care* **2,** 122–141 (2013).
35. Bollong, M. J. *et al.* Small molecule-mediated inhibition of myofibroblast transdifferentiation for the treatment of fibrosis. *Proceedings of the National Academy of Sciences* **114,** 4679–4684 (2017).
36. Quach, N. L., Biressi, S., Reichardt, L. F., Keller, C. & Rando, T. A. Focal Adhesion Kinase Signaling Regulates the Expression of Caveolin 3 and β1 Integrin, Genes Essential for Normal Myoblast Fusion. *Molecular Biology of the Cell* **20,** 3422–3435 (2009).
37. Clemente, C. F. M. Z., Corat, M. A. F., Saad, S. T. O. & Franchini, K. G. Differentiation of C 2C 12myoblasts is critically regulated by FAK signaling. *American Journal of Physiology-Regulatory, Integrative and Comparative Physiology* **289,** R862–R870 (2005).
38. Bachmann, P. & Hinrichsen, K. Semiautomated evaluation of morphometric data of myoblasts and myotubes and the calculation of the relative DNA content with the television texture analysis system (TAS). *Histochemistry* **69,** 233–242 (1980).

39. Lassalle, B., Gautron, J., Martelly, I. & Le Moigne, A. Image analysis of rat satellite cell proliferation in vitro. *Cytotechnology* **2,** 213–224 (1989).
40. Treiser, M. D. *et al.* Cytoskeleton-based forecasting of stem cell lineage fates. *Proc. Natl. Acad. Sci. U.S.A.* **107,** 610–615 (2010).
41. Kilian, K. A., Bugarija, B., Lahn, B. T. & Mrksich, M. Geometric cues for directing the differentiation of mesenchymal stem cells. *Proc. Natl. Acad. Sci. U.S.A.* **107,** 4872–4877 (2010).
42. Swift, J. *et al.* Nuclear lamin-A scales with tissue stiffness and enhances matrix-directed differentiation. *Science* **341,** 1240104 (2013).
43. Shin, H. *et al.* Focal Adhesion Assembly Induces Phenotypic Changes and Dedifferentiation in Chondrocytes. *J. Cell. Physiol.* **231,** 1822–1831 (2016).
44. Connelly, J. T., García, A. J. & Levenston, M. E. Interactions between integrin ligand density and cytoskeletal integrity regulate BMSC chondrogenesis. *J. Cell. Physiol.* **217,** 145–154 (2008).
45. Vasilopoulos, Y., Gkretsi, V., Armaka, M., Aidinis, V. & Kollias, G. Actin cytoskeleton dynamics linked to synovial fibroblast activation as a novel pathogenic principle in TNF-driven arthritis. *Annals of the Rheumatic Diseases* **66 Suppl 3,** iii23–8 (2007).
46. Dalby, M. J. Cellular response to low adhesion nanotopographies. *Int J Nanomedicine* **2,** 373–381 (2007).
47. Newman, P. *et al.* Relationship between nanotopographical alignment and stem cell fate with live imaging and shape analysis. *Sci. Rep.* **6,** 37909 (2016).
48. Wong, V. W. *et al.* Focal adhesion kinase links mechanical force to skin fibrosis via inflammatory signaling. *Nat Med* **18,** 148–152 (2011).
49. Castillo, A. B. *et al.* Focal Adhesion Kinase Plays a Role in Osteoblast Mechanotransduction In Vitro but Does Not Affect Load-Induced Bone Formation In Vivo. *PLoS ONE* **7,** e43291–11 (2012).
50. Salasznyk, R. M., Klees, R. F., Williams, W. A., Boskey, A. & Plopper, G. E. Focal adhesion kinase signaling pathways regulate the osteogenic differentiation of human mesenchymal stem cells. *Exp. Cell Res.* **313,** 22–37 (2007).
51. Wang, I.-N. E. *et al.* Role of osteoblast-fibroblast interactions in the formation of the ligament-to-bone interface. *J. Orthop. Res.* **25,** 1609–1620 (2007).
52. Gautrot, J. E. *et al.* The Nanoscale Geometrical Maturation of Focal Adhesions Controls Stem Cell Differentiation and Mechanotransduction. *Nano Lett.* **14,** 3945–3952 (2014).
53. Changede, R., Cai, H., Wind, S. & Sheetz, M. P. Ligand Geometry Controls Adhesion formation via Integrin Clustering. *bioRxiv* (2018). doi:10.1101/435826
54. Li, B., Moshfegh, C., Lin, Z., Albuschies, J. & Vogel, V. Mesenchymal stem cells exploit extracellular matrix as mechanotransducer. *Sci. Rep.* **3,** 2425 (2013).
55. Trappmann, B. *et al.* Extracellular-matrix tethering regulates stem-cell fate. *Nature Materials* **11,** 642–649 (2012).
56. Oria, R. *et al.* Force loading explains spatial sensing of ligands by cells. *Nature* 1–20 (2017). doi:10.1038/nature24662

57. Guillaume-Gentil, O. *et al.* Tunable Single-Cell Extraction for Molecular Analyses. *Cell* **166,** 506–516 (2016).
58. Lindley, D. V. On a Measure of the Information Provided by an Experiment. *The Annals of Mathematical Statistics* **27,** 986–1005 (1956).
59. Chaloner, K. & Verdinelli, I. Bayesian Experimental Design: A Review. *Statistical Science* **10,** 273–304 (1995).
60. Stormonth-Darling, J. M., Saeed, A., Reynolds, P. M. & Gadegaard, N. Injection Molding Micro- and Nanostructures in Thermoplastic Elastomers. *Macromol. Mater. Eng.* **301,** 964–971 (2016).
61. Yan, X.-Z. *et al.* Effects of continuous passaging on mineralization of MC3T3-E1 cells with improved osteogenic culture protocol. *Tissue Engineering Part C: Methods* **20,** 198–204 (2014).
62. Caicedo, J. C. *et al.* Data-analysis strategies for image-based cell profiling. *Nat Meth* **14,** 849–863 (2017).
63. Kamentsky, L. *et al.* Improved structure, function and compatibility for CellProfiler: modular high-throughput image analysis software. *Bioinformatics* **27,** 1179–1180 (2011).
64. Zhan, X., Patterson, A. D. & Ghosh, D. Kernel approaches for differential expression analysis of mass spectrometry-based metabolomics data. *BMC Bioinformatics* **16,** 77 (2015).
65. Warnes, G. R. *et al.* gplots: Various R programming tools for plotting data. *R package version* **2,** 1 (2009).
66. Maechler, M., Rousseeuw, P., Struyf, A., Hubert, M. & Hornik, K. cluster: Cluster Analysis Basics and Extensions. (2017).
67. Wei, T. *et al.* **corrplot: Visualization of a Correlation Matrix**. (2017).
68. Kuhn, M. Building Predictive Models in R Using the caret Package. *Journal of Statistical Software* **28,** 1–26 (2008).
69. Bürkner, P.-C. brms: An RPackage for Bayesian Multilevel Models Using Stan. *Journal of Statistical Software* **80,** 1–28 (2017).
70. Team, R. R: A language and environment for statistical computing. (2017).
71. Wickham, H. *ggplot2: Elegant Graphics for Data Analysis*. (Springer-Verlag New York, 2009).
72. Akima, H. & Gebhardt, A. akima: Interpolation of Irregularly and Regularly Spaced Data.